



UPPSALA  
UNIVERSITET

# Probing the Solar Wind Evolution with Kinetic Waves

by

Joan Jordi Boldú-O'Farrill Treviño

November 14, 2023

Department of Physics and Astronomy  
Uppsala University  
SE-75120 Uppsala, Sweden

*Submitted to the Faculty of Science and Technology, Uppsala University  
in partial fulfillment of the requirements for the degree of  
Licentiate of Philosophy in Physics*





## Abstract

Charged particles constantly stream outward from the Sun to fill the solar system. These particles, consisting mainly of protons and electrons, form a plasma called the solar wind. The solar wind interacts with every celestial body in the solar system, giving rise to different phenomena, such as the auro-ras observed at high latitudes on Earth or disruption of the systems onboard artificial satellites.

The general structure of the solar wind has been established several decades ago, however we still do not fully understand how the solar wind properties, like temperature and velocity distribution, evolve as it propagates outward in the solar system. Observations of these properties cannot be explained from a conventional fluid description. In a system approximated as a fluid, particle collisions dictate its thermodynamic state. However, the solar wind is a weakly collisional plasma that deviates from thermodynamic equilibrium. Therefore, the radial evolution of the solar wind properties must be driven by different processes. In particular, wave-particle interactions are an important regulator of the solar wind properties, because of the strong connection between the electromagnetic fields and the charged particles.

In this thesis, we probe how the velocity distribution of solar wind particles evolves as it travels from the Sun to the Earth. Specifically, we study the contribution of waves on the observed solar wind properties at different distances and how these waves can affect the interplanetary environment. We focus on two types of plasma waves frequently observed in the solar wind, Langmuir and ion-acoustic waves. We present their occurrence rates at different heliocentric distances and suggest wave generation mechanisms based on Solar Orbiter observations. We show that Langmuir waves in the unperturbed solar wind are more commonly observed in regions where the magnetic field magnitude is lower than the background value. Furthermore, we also find that the occurrence rate of ion-acoustic waves is increased in the ramp regions of interplanetary shocks observed at different heliocentric distances, compared to the ion-acoustic wave occurrence rate in the unperturbed solar wind.







## List of papers

This licentiate thesis is based on the following papers:

### Paper I

**Boldú, J.J.**, Graham, D. B., Khotyaintsev, Y. V., Morooka, M., André, M., Karlsson, T., Souček, J., Píša, D. & Maksimovic, M. (2023). Langmuir waves associated with magnetic holes in the solar wind. *Astronomy and Astrophysics: Solar Orbiter First Results (Nominal Mission Phase)*, 674, A220. [doi.org/10.1051/0004-6361/202346100](https://doi.org/10.1051/0004-6361/202346100)

### Paper II

**Boldú, J.J.**, Graham, D. B., Khotyaintsev, Y. V., Morooka, M., André, M., Dimmock, A., Souček, J., Píša, D. & Maksimovic, M. Ion-acoustic waves associated with interplanetary shocks.

In preparation

Reprints were made with permission from the publisher.

# Contents

<b>1</b>	<b>Introduction</b>	<b>1</b>
<b>2</b>	<b>Solar Wind</b>	<b>3</b>
2.1	The solar wind and its scales . . . . .	3
2.2	Kinetic view of the solar wind . . . . .	9
2.3	Solar wind phenomena . . . . .	12
2.3.1	Interplanetary shocks . . . . .	14
2.3.2	Radio bursts . . . . .	14
2.3.3	Magnetic holes . . . . .	16
<b>3</b>	<b>Plasma Waves</b>	<b>19</b>
3.1	Basic plasma wave theory . . . . .	19
3.2	Electrostatic waves . . . . .	22
3.2.1	Langmuir waves . . . . .	25
3.2.2	Ion-acoustic waves . . . . .	26
3.3	Kinetic instabilities . . . . .	29
<b>4</b>	<b>Effect of electrostatic waves on the evolution of the solar wind</b>	<b>32</b>
<b>5</b>	<b>The Solar Orbiter Mission</b>	<b>34</b>
5.1	The Radio and Plasma Waves Instrument . . . . .	35
5.2	Other in-situ experiments . . . . .	36
<b>6</b>	<b>Outlook</b>	<b>38</b>
<b>7</b>	<b>Acknowledgements</b>	<b>40</b>





# 1 Introduction

The solar wind is a stream of charged particles expelled constantly from the Sun. It operates as an extension of the solar atmosphere's outermost layer, the corona, creating the heliosphere. The heliosphere reaches far beyond the orbit of Pluto and every astronomical object inside it interacts with the solar wind, generating a variety of interplanetary phenomena.

When particle collisions are the dominant processes, a system is brought to thermodynamic equilibrium and it can be described by means of average quantities, such as bulk velocity and temperature, of the particles constituting a fluid. In this manner, the evolution of the corona and solar wind is usually described with a magnetohydrodynamic (MHD) model accounting for a steady coronal expansion. Although this model provides an insightful view of the overall structure of the solar wind, it cannot explain the observed velocity distributions of the particles. Moreover, the solar wind temperature profiles at different distances deviate from that expected from an adiabatic expansion (Cranmer et al., 2009), meaning that some heating mechanisms must be active. Because the mean free path of the particles in the inner heliosphere is larger than the characteristic size of the system, collisions are rare. Therefore, solar wind models cannot rely on collisions to accurately explain its evolution and it is necessary to investigate how the particles are distributed in velocity space. Investigation of the particle distributions is the basis of the kinetic approach to describe the solar wind properties and their evolution.

When describing the solar wind using kinetic models, mechanisms that can have similar effects to particle collisions arise. Notably, the interaction between particles and waves that readily occur in the solar wind can play an important role in shaping the particle distributions. Nevertheless, the influence of various wave modes on the solar wind distributions is still not fully understood, much less how their effect varies with radial distance. With the arrival of newer space missions, like Solar Orbiter, it is now possible to use waves, described using the kinetic approach, to probe the evolution of the solar wind at different heliocentric distances. Kinetic waves such as whistlers, Langmuir, ion-cyclotron, lower-hybrid, and ion-acoustic waves, frequently occur in the solar wind and potentially contribute to the solar wind evolution. Knowing how these waves are generated, interact with the particles, and regulate the kinetic features of the solar wind is, therefore, fundamental to understand-

ing the evolution of the solar wind. In this thesis, we probe the evolution of the solar wind by characterizing and quantifying two types of common kinetic waves in the solar wind, namely Langmuir waves and ion-acoustic waves.

In Chapter 2, we describe the solar wind, its source, and its properties under the scrutiny of different frameworks. In Chapter 3, we describe different types of waves that can be present in a plasma. We focus on electrostatic waves present in the solar wind. We show, in Chapter 4, the relation of the observed electrostatic waves with various phenomena commonly occurring in the solar wind at different heliocentric distances. Then, in Chapter 5, we describe the Solar Orbiter spacecraft and its in-situ experiments utilized to probe the solar wind evolution. We conclude with Chapter 6, where we include an outlook of future efforts needed to understand better the role that kinetic waves play in shaping the evolution of the solar wind.

## 2 Solar Wind

One of the first mentions of the existence of a stream of particles originated in the Sun was provided by Sir Arthur Eddington in 1910 . He proposed ions streaming from the Sun as an explanation of the observed shape of cometary tails (Eddington, 1910). This already provided evidence that the Sun not only interacts with different bodies by emitting electromagnetic radiation, but also by means of particle radiation. This stream of particles was later named the solar wind and has been a crucial research topic in many disciplines such as space weather and space physics due to its strong interaction with different interplanetary bodies.

In this chapter we provide a general understanding of the solar wind. In section 2.1 we introduce the solar wind from its origin at the solar corona to the interplanetary medium. We present the solar wind under two different frameworks: magnetohydrodynamics and kinetic theory. In section 2.2, we focus in the kinetic picture of the solar wind and describe how its particles are typically distributed according to their probability to be found moving at a given velocity. Next, in section 2.3, we provide evidence of the dynamic nature of the solar wind by analyzing different transient structures common to it, such as interplanetary shocks, radio bursts, and magnetic holes.

### 2.1 The solar wind and its scales

It was shown in 1958 by Eugene Parker that the hot outermost layer of the Sun, the corona, cannot sustain hydrostatic equilibrium. The pressure-gradient force overcomes gravity and leads to a radial acceleration of the coronal plasma to supersonic velocities (Parker, 1958). Because of this coronal expansion, the Sun's atmosphere extends throughout the interplanetary medium, forming the heliosphere. As we will later see, the solar corona and solar wind can be analyzed at different temporal and spatial scales. In the first models the solar corona was assumed to be a stable system at the largest scales (Chapman S., 1957). For the corona to be in hydrostatic equilibrium the pressure far from the origin should not be greater than the interstellar medium pressure (Parker, 1958). However, as noted by Parker, the pressure at infinity in the hydrostatic model was non-zero and certainly not small enough to support the equilibrium assumption.

In Parker's model a stationary hydrodynamic expansion of the corona is

considered. To calculate the plasma expansion velocity ( $v$ ) in terms of the radial distance ( $r$ ) we first consider the corona under the influence of gravity and pressure, neglecting the effects of the magnetic field. The solution to the equation of motion is then

$$\frac{v^2}{V_s^2} - \ln\left(\frac{v^2}{V_s^2}\right) = 4\ln\left(\frac{r}{r_c}\right) + 4\frac{r_c}{r} + v_0, \quad (1)$$

with  $v_0$  being an integration constant. To make the equation of motion solvable analytically, an isothermal corona was assumed. Then, the speed of sound is defined as  $V_s = \sqrt{p/\rho_m}$ , where  $p$  is the pressure and  $\rho_m$  the mass density. The critical distance  $r_c$  defines the distance at which the solar wind reaches the isothermal speed of sound.

There are five types of solutions associated with eq. (1), shown in the left panel on Fig. 1. Solutions of type 1, besides being double valued, never cross the critical surface and are bounded to the corona. Solutions of type 2 are also double valued and are not connected to the corona. Solutions of type 3 require supersonic plasma below the critical surface. This type of solution can also be ruled out, as such high coronal motions are not observed (Hundhausen, 1972). Type 4 solutions predict a subsonic flow passed the critical point. This kind of flow was termed the “solar breeze” (Chamberlain, 1961). Finally, type 5 solutions correspond to a supersonic flow beyond  $r_c$ . This is the solar wind solution. The solar breeze was proven to be unstable (Velli, 1994), but the definitive evidence pointing toward the solar wind solution was provided by the first in-situ measurements, which showed that the interplanetary plasma travels at supersonic speed (Gringauz, 1960; Neugebauer & Snyder, 1962).

This steady expansion model of the corona is insightful to understand the out-flowing nature of the solar wind, however it is not yet complete. Formed by multiple charged particles, a plasma strongly interacts with electric and magnetic fields. The Sun generates a coronal magnetic field that extends throughout the heliosphere, becoming the interplanetary magnetic field (IMF). Therefore, we need to extend Parker’s model based on hydrodynamics to a more appropriate framework, namely the MHD framework.

In the MHD approach we consider the plasma as a single-fluid resulting from the contribution of all particle species’ fluid equations. To apply the MHD-fluid description of a plasma we need to know at which scales it is a valid representation of the system.

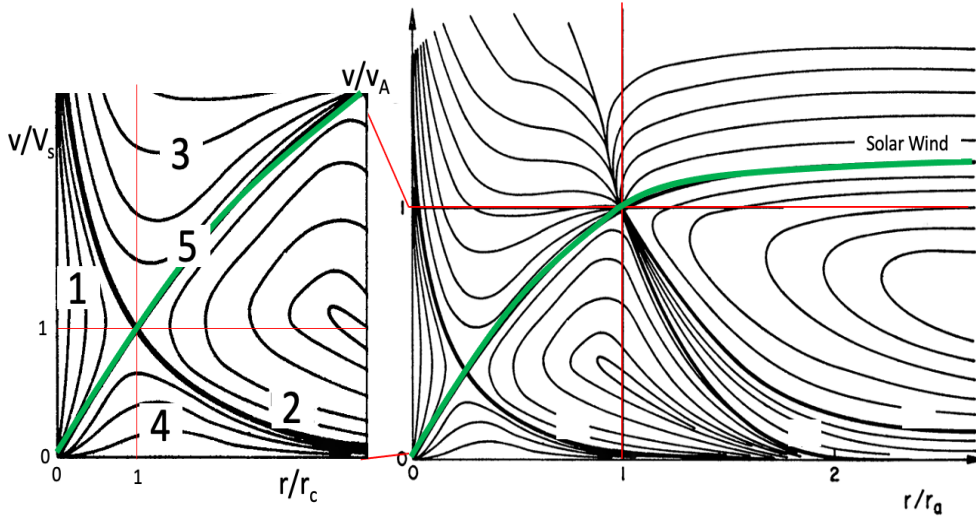


Figure 1: Solutions to the MHD model of the coronal expansion. The green line (solution 5) corresponds to the solar wind solution. In the left panel, solutions are presented with respect to the sound speed  $V_s$  and sound-speed critical surface  $r_c$ . Solutions 1-4 are not physical or not supported by observations. In the right figure, solutions with respect to the Alfvén speed  $V_A$  and the Alfvén critical surface  $r_A$ . The third critical point, related to the fast magnetosonic speed, is close to  $r_A$  and is not distinguishable in the figure. The solar wind solution passes through all critical points. Adapted from Weber & Davis (1967).

When a charged particle is immersed in a magnetic field, it will start to gyrate around the field lines. The radius of gyration is called the gyroradius or Larmour radius  $\rho_L$  and depends on the particle’s mass  $m$ , charge  $|q|$ , the perpendicular-to-magnetic field velocity  $v_\perp$  and the magnetic field strength  $B$  such that

$$\rho_L = \frac{mv_\perp}{|q|B}. \quad (2)$$

We also introduce the inertial length, which is defined as

$$d = c/\omega_p, \quad (3)$$

where  $c$  is the speed of light and  $\omega_p$  is the plasma frequency, defined as

$$\omega_p^2 = \frac{nq^2}{\epsilon_0 m}, \quad (4)$$

where  $n$  is the number density and  $\epsilon_0$  the permittivity of free space. This

is the frequency at which particles in a plasma oscillate due to electric fields generated by small charge separation. Since it depends on the particle's mass, there will be a  $\omega_p$  associated to each species. Typical values of solar wind scales and properties at 1 AU are shown in Table 2.1. It is important to note, that these parameters vary with distance, and depend on the source of the solar wind in the corona.

Property	electrons	protons
Inertial length ( $d$ )	3 km	140 km
Plasma frequency ( $f_p$ )	20 kHz	500 Hz
Gyroradius ( $\rho_L$ )	2 km	160 km
Gyrofrequency ( $f_g$ )	100 Hz	50 Hz
Number density ( $n_s$ )	10 cm <sup>3</sup>	10 cm <sup>3</sup>
Temperature ( $T_s$ )	1.44×10 <sup>5</sup> K	1.0×10 <sup>5</sup> K
Magnetic field magnitude ( $ B $ )	5 nT	
Proton collisional mean free path ( $\lambda_{mfp}$ )	3 AU	
Debye length ( $\lambda_D$ )	10 m	

Table 1: Properties of the solar wind around 1 AU. (Verscharen et al., 2019; Newbury et al., 1998). The ordinary frequencies  $f$  are related to the angular frequencies  $\omega$  by  $\omega = 2\pi f$ .

For the MHD description to be valid, the length scales at which we study the plasma must be much greater than the maximum between  $\rho_L$  and  $d$ . The upper bound is defined by the characteristic length ( $L$ ) of the system. For the heliosphere  $L \sim 90$  AU, and for the inner heliosphere  $L \sim 1$  AU.

Now that we defined the scales we are interested in, we analyze the behavior of the magnetic field. The rate of change of the magnetic field  $\mathbf{B}$  is governed by convection and diffusion effects given by

$$\frac{\partial \mathbf{B}}{\partial t} = \nabla \times (\mathbf{V} \times \mathbf{B}) + \frac{1}{\mu_0 \sigma} \nabla^2 \mathbf{B}, \quad (5)$$

where  $\mu_0$  is the permeability of free space,  $\mathbf{V}$  the velocity of the plasma, and  $\sigma$  is the conductivity of the plasma. The ratio between the convection and diffusion can be roughly estimated by the magnetic Reynolds number, defined as

$$R_m = \mu_0 \sigma V L. \quad (6)$$

For values of  $R_m \ll 1$  diffusion dominates and the magnetic field will dissipate

through the plasma. For  $R_m \gg 1$  convection dominates and the plasma will be embedded in the magnetic field lines. This latter case is the condition for the frozen field theorem, since the magnetic flux acts as if it was frozen into the plasma. At the spatial scales analyzed and for the high solar wind conductivity, the frozen field theorem holds. Then, we just need to understand if it is the magnetic field or the plasma which governs the motion. For this we define the plasma  $\beta$  as the ratio of the plasma pressure and the magnetic pressure. If  $\beta > 1$  the motion is primarily governed by the plasma and by the magnetic field for  $\beta < 1$ . Now, we can include the effects of the magnetic field into the solar wind model. We start by taking into account the rotation of the Sun.

In a coordinate frame  $(r, \phi, \theta)$  rotating at the angular velocity of the Sun  $\omega_\odot$ , the solar wind will follow a trajectory with radial ( $v_r = v$ ) and azimuthal ( $v_\phi = -\omega_\odot r \sin \theta$ ) components. As seen from eq. (1), at  $r \gg r_c$  the solar wind velocity is approximately constant ( $v = v_\infty$ ). Then, the geometry of the solar wind streamlines, in this frame, will be of the form

$$(r - r_c) = -\frac{v_\infty}{\omega_\odot r \sin \theta}(\phi - \phi_0), \quad (7)$$

with the initial azimuthal position at  $r_c$  being  $\phi_0$ . This trajectory has the shape of an Archimedean spiral. As a result, in the rotating frame, the solar wind flow streamlines are not straight, but they spiral out. Here is where the application of the frozen field theorem is of great importance. Since the magnetic field and plasma streamlines are tightly related, the shape of the former will be the same as the latter. In absence of the Sun's rotation, the magnetic field lines will be stretched radially as the solar wind expands. Taking into account the rotation, the IMF will be stretched and twisted into a spiral shape. This IMF configuration is called the Parker spiral.

The last step is to include the magnetic field forces into Parker's solution. The equation of motion is now

$$\rho_m \left( v_r \frac{dv_r}{dr} - \frac{v_\phi^2}{r} \right) = \frac{dp}{dr} - \rho_m \frac{GM_\odot}{r^2} - \frac{B_\phi}{\mu_0 r} \frac{d}{dr}(r B_\phi), \quad (8)$$

with  $\mu_0$  being the permeability of free space,  $GM_\odot$  the Sun's gravitational parameter and  $B_\phi$  the azimuthal component of the magnetic field. The solutions of eq. (8) are shown on the right panel in Fig. 1. Again, the acceptable solution is the solar wind representation, corresponding to the central green line that



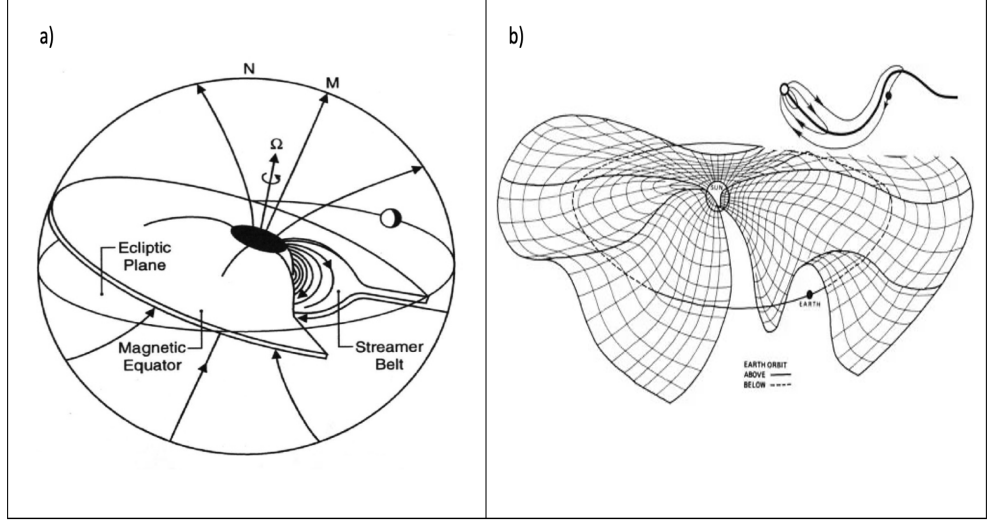


Figure 2: (a) Simplified version of the IMF. The coronal magnetic field is stretched by the plasma, forming a current sheet near the solar equator where the magnetic field polarity reverses. Taken from Russell (2013) (b) A 3D view of the heliocentric current sheet extending throughout the inner heliosphere. Taken from Council et al. (2004).

crosses all the critical points. In the hydrodynamic solution first considered by Parker, the critical velocity was  $V_s$ . In a magnetized plasma, signals cannot only travel as fluid pressure waves, but as magnetic pressure waves, called Alfvén waves, or as a combination of both. As a consequence, there exist three critical points, corresponding to the slow magnetosonic ( $V_{sm}$ ), Alfvén ( $V_A$ ) and fast magnetosonic ( $V_{fm}$ ) speeds. The distance at which  $v = V_A$  is called the Alfvén critical surface ( $r_A$ ) and has been adopted as the boundary between the corona and the solar wind. Below this surface  $\beta < 1$ , the magnetic field dominates the motion and the plasma is bounded to the corona. Beyond  $r_A$  the plasma dominates and the radial expansion of the solar wind at superalfvénic and supersonic speeds takes place.

Because the IMF is stretched by the solar wind, a current sheet is formed in the boundary region where the magnetic field changes polarity, as depicted in Fig. 2(a). This current sheet that extends throughout the heliosphere is the heliospheric current sheet (HCS). In reality, the Parker spiral is not confined to the Sun's equatorial plane. The HCS turns up and down dividing the heliosphere into magnetic sectors of different polarity, and resembles a waving table cloth or a ballerina skirt as shown in Fig. 2(b).

As a consequence of the solar wind expansion, its density decreases with radial distance. Electron and ion temperatures also decrease with distance but at a more moderate rate (Verscharen et al., 2019). This expansion model gives a useful first-order description of the evolution of the solar wind. However, this model cannot account for many of the observed features of the solar wind. For example, observed faster solar wind streams do not fit this model (Leer, 1982; Hansteen, 2012). New models have come to light trying to reconcile the observations of fast solar winds and unidentified heating mechanisms (McComas, 2007; Cranmer, 2012), many of which are not based on MHD, but on kinetic theory (Jockers, 1970; Lemaire, 1971). Nonetheless, any theory able to explain the solar wind acceleration and heating, must be consistent with the observed velocity distributions and how they evolve as the solar wind propagates radially from the Sun (Maksimovic et al., 2005; Matteini et al., 2007; Štěpán Štverák et al., 2009). Small-scale processes occurring throughout the solar wind, such as wave-particle interactions, may contribute to the solar wind evolution. In the next section we focus on the kinetic description of the solar wind, that is, at scales comparable to or smaller than particle inertial lengths and gyroradii, where the single-fluid description is no longer valid.

## 2.2 Kinetic view of the solar wind

As a plasma, the solar wind exhibits collective behavior of charged particles that are governed by electromagnetic forces. Although, individual particles have a charge, at macroscopic scales the system is quasi-neutral and the plasma has zero net charge. The minimum length at which quasi-neutrality holds, and thus satisfy the definition of plasma, is called the Debye length, which is given by

$$\lambda_D^2 = \frac{\epsilon_0 \kappa_B T_e}{n q^2}, \quad (9)$$

where  $\kappa_B$  is the Boltzmann constant and  $T_e$  the electron temperature. This length provides a lower limit where the kinetic description of the solar wind is valid. The typical solar wind Debye length at 1 AU is around 10 m (Verscharen et al., 2019), becoming shorter with decreasing heliocentric distance.

Using statistical mechanics, the particles in a plasma can be represented by a probability distribution function  $f(\mathbf{r}, \mathbf{v}, t)$ , rather than individual particles; each governed by their own equation of motion. In the absence of collisions between particles the evolution of the distribution function is described by the

Vlasov equation:

$$\frac{\partial f_s}{\partial t} + \mathbf{v} \cdot \nabla f_s + \frac{q_s}{m_s} (\mathbf{E} + \mathbf{v} \times \mathbf{B}) \cdot \nabla_v f_s = 0, \quad (10)$$

where the subscript  $s$  indicates the particle species in question,  $\mathbf{E}$  and  $\mathbf{B}$  are the electric and magnetic fields respectively. The symbol  $\nabla_v$  means the gradient over velocity space.

Multiplying the distribution function by powers of the velocity and integrating over velocity space we can define useful macroscopic quantities. These quantities are called the moments of the distribution and can be used to analyze the plasma as a multiple-fluid, where each particle species has its own moment equations. The first four moments are:

1. Zeroth moment: number density  $\rightarrow n_s = \int_v f_s(\mathbf{r}, \mathbf{v}, t) d^3v$
2. First moment: bulk velocity  $\rightarrow \mathbf{U}_s = \frac{1}{n_s} \int_v \mathbf{v} f_s(\mathbf{r}, \mathbf{v}, t) d^3v$
3. Second moment: Pressure tensor  $\rightarrow \overleftrightarrow{P}_s = m_s \int_v (\mathbf{v} - \mathbf{U}_s)(\mathbf{v} - \mathbf{U}_s) f_s(\mathbf{r}, \mathbf{v}, t) d^3v$
4. Third moment: Heat-flux tensor  $\rightarrow \overleftrightarrow{Q}_s = m_s \int_v (\mathbf{v} - \mathbf{U}_s)(\mathbf{v} - \mathbf{U}_s)(\mathbf{v} - \mathbf{U}_s) f_s(\mathbf{r}, \mathbf{v}, t) d^3v$

where  $m_s$  is the mass of species  $s$ .

A plasma in thermodynamic equilibrium will exhibit a distribution of Gaussian shape, called a Maxwellian distribution. Normally, thermodynamic equilibrium is achieved by collisions in the plasma. In the solar wind the typical proton collisional mean free path ( $\lambda_{mfp}$ ) is of the order of  $\sim 3$  AU (Verscharen et al., 2019). Since the characteristic size of the system at the inner heliosphere ( $\sim 1-3$  AU) is of the same order as  $\lambda_{mfp}$ , collisions play a minor role in the evolution of the distribution function and it is said that the plasma is weakly collisional. This is an important statement, because in a collisionless or weakly collisional plasma the distributions can deviate significantly from a Maxwellian distribution. Such deviations can result in the distributions being unstable to kinetic instabilities. We will discuss in chapter 3 that wave-particle interactions can mimic the role of collisions by restoring an unstable distribution to a stable state, which is not necessarily in thermodynamic equilibrium.

The spread of the velocity distribution function (VDF) can be represented by the thermal velocity ( $v_{th,s} = \sqrt{\kappa_B T_s / m_s}$ ), with  $T_s$  being the temperature

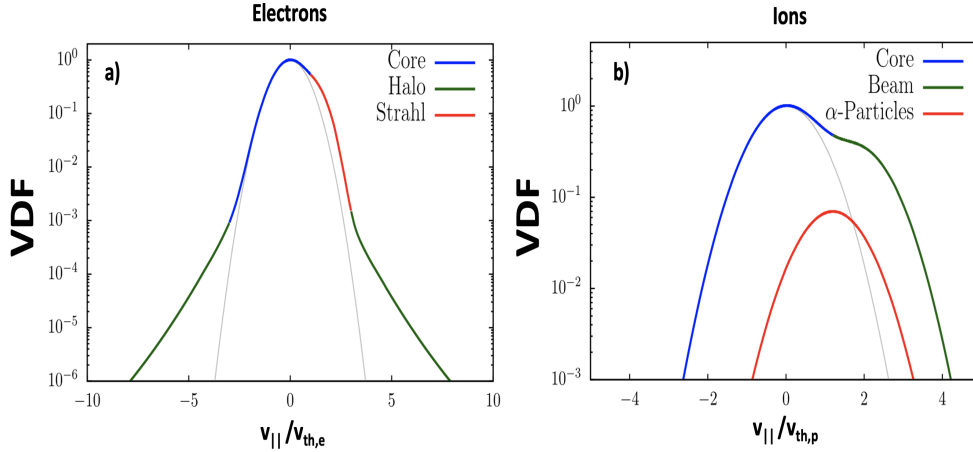


Figure 3: Typical solar wind VDFs along the parallel-to-magnetic field direction. (a) electron VDF. The solar wind electron VDF usually consists of three population. A bi-Maxwellian core, an isotropic halo and a field aligned strahl. (b) Ion VDF. The solar wind ion VDF usually contains two proton populations and an  $\alpha$ -particle population. The electron and ion velocities are normalized by the thermal velocities of electrons and protons respectively. Taken from Verscharen et al. (2019).

of species  $s$ . A typical VDF, in the direction along the magnetic field, of solar wind electrons (subscript  $e$ ) is shown in Fig. 3(a). Three components are usually present. First, a core population exhibiting an approximately Maxwellian distribution with  $v_{th,e} \sim 1300$  km/s and that constitutes around 95 % of the total  $n_e$ . Second, a population with increased number of electrons at higher energies, closely exhibiting a Lorentzian or  $\kappa$ -distribution and  $v_{th,e} \lesssim 3500$  km/s, called the halo (Maksimovic et al., 1997; Štěpán Štverák et al., 2009). Third, a population of electrons aligned with the magnetic field and propagating outward from the Sun with bulk energies  $\sim 100$  eV, called the strahl (Rosenbauer et al., 1977; Verscharen et al., 2019).

The ion VDF, shown in Fig. 3(b) consists mainly of protons (subscript  $p$ ), accounting for almost 95% of solar wind ions, but a population of  $\alpha$ -particles is often present (Ogilvie, 1975; Verscharen et al., 2019). Heavier ions are less abundant, but can be also present (Bame et al., 1975). The proton distribution often exhibits a two-stream population, deviating from a Maxwellian distribution. This distribution is formed by thermal core protons and a faster beam, mostly field-aligned and directed anti-sunward (Feldman et al., 1974; Alterman et al., 2018). At least in the inner heliosphere, it is also common

to observe proton distributions with larger thermal energies in the direction perpendicular to the magnetic field ( $T_{\perp}$ ) than parallel to it ( $T_{\parallel}$ ). Although, periods when  $T_{\parallel} > T_{\perp}$  are also observed, they happen less frequently (Matteini et al., 2007). When the particles are not distributed equally among velocity space directions, the distribution is referred as anisotropic. Anisotropies in the VDFs are common sources of instabilities that can lead to wave growth.

The shape of the VDFs is heavily influenced by plasma waves and vice versa. How these distributions change as they travel away from the Sun play a primary role dictating the evolution of the solar wind bulk parameters.

### 2.3 Solar wind phenomena

We start this section by considering time variations to the solar wind model. Due to various effects such as the Sun’s differential rotation, and internal plasma circulation (Hazra & Nandy, 2016), the magnetic structure of the Sun varies over an 11-year cycle (Babcock, 1961). Conventionally, this cycle begins at solar minimum, when the magnetic field configuration is closer to a dipole. As the cycle continues, a stage of solar maximum is reached, where the magnetic field configuration becomes more complex and can no longer be described as dipole. Consequently, the solar wind is classified into fast wind, streaming from coronal holes where the IMF lines are ‘open’, and slow wind emerging from streamer regions. During solar minimum the fast wind is mostly confined to the polar coronal holes (McComas et al., 1998), and the slow wind to the streamer belt near the solar equator (Zhao & Hundhausen, 1981; Gosling et al., 1981), as shown in Fig. 4(a). During solar maximum, the coronal holes appear at lower latitudes and streamer regions at higher ones. This causes fast and slow flows to be less localized and the overall structure of the solar wind is less predictable. This is exemplified in Fig. 4(b).

The slow solar wind is on average denser and more variable than the fast wind, with velocities below  $\sim 500$  km/s. The fast solar wind, traveling at velocities around 500 km/s and 800 km/s (Verscharen et al., 2019), exhibits more deviations from a Maxwellian distribution in its VDFs compared to the slow wind (Marsch, 2006, 2018). Furthermore, transient events, typically associated with solar maximum, exist in the solar wind and have velocities that can vary from a few hundred km/s up to 2000 km/s (Verscharen et al., 2019). One example are coronal mass ejections (CME), which are eruptive events where a significant increase in the plasma expelled into the interplanetary

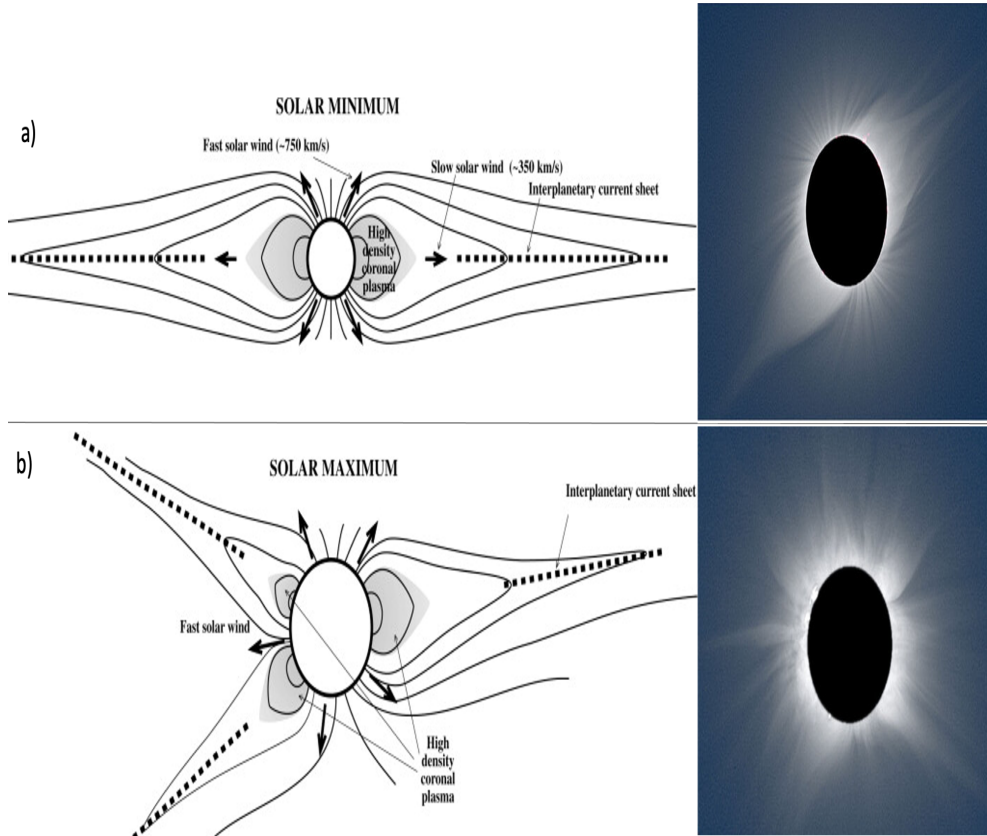


Figure 4: Two configurations of the solar corona and IMF during a solar cycle. (a) Solar minimum configuration. The fast solar wind is mostly confined to the coronal holes located near polar latitudes; the slow solar wind streams from a belt close to the equator. To the right a picture of a solar eclipse during solar minimum. (b) Solar maximum configuration. The coronal magnetic field gets tangles as an effect of the Sun's differential rotation. The coronal holes and streamer belts are no longer localized at the poles and equator, respectively. To the right a picture of a solar eclipse during solar maximum. Taken from Lyons (2003). Photographs taken from (Dikpati et al., 2016).

medium takes place (Low, 1996). Another example of solar wind transient events are solar flares. Solar flares occur in regions of high solar activity where an enhancement of electromagnetic emissions is produced (Sweet, 1969). In contrast with the longer 11-year solar cycle, transient events are shorter lived, and they are more frequent during solar maximum. Solar wind transient events are of special interest, because of their extreme plasma and magnetic field conditions, as well as their potential space weather effects (Baker & Kanekal, 2008). Here, we present some of the phenomena related to transient events

and other solar wind processes that are often associated with plasma waves that can influence the evolution of the solar wind and modify its VDF.

### 2.3.1 Interplanetary shocks

On certain occasions, the fast wind can reach regions of slow wind in the Parker spiral. At the boundary of the fast and slow winds, a stream interaction region (SIR) is formed (Richardson, 2018). At a SIR the plasma is compressed and can potentially generate a shock wave. A shock wave in the interplanetary medium is called an interplanetary (IP) shock. These shocks are common in the solar wind, especially during periods of high solar activity, where the coronal holes and streamer regions occur at closer latitudes (Kilpua et al., 2015). Another source of IP shocks are CMEs. Because of the high velocities at which the plasma can be expelled, shock waves are often formed in the leading edge of CMEs.

An IP shock can be characterized by a few parameters. The Mach number ( $M$ ) relates the upstream velocity with a characteristic speed, such as Alfvén speed or fast magnetosonic speed; the angle  $\theta_{BN}$  formed by the upstream magnetic field and the vector normal to the surface of the shock; the velocity of the shock front ( $V_{sh}$ ); or the compression ratio between upstream and downstream regions. An example of an IP shock observed by Solar Orbiter at 0.8 AU is shown in Fig. 5. Signatures of an IP shock include a discontinuity or “jump” in the magnetic field strength, density and velocity, as seen in panels (a),(b) and (c), respectively.

Although an MHD analysis can provide an insightful description of the conditions that lead to the formation of IP shocks, the processes occurring near the shocks are of kinetic nature. For instance, the generation of kinetic waves, that in turn affect the VDFs (Fitzenreiter, 2003; Goodrich et al., 2019). Moreover, ion-acoustic waves may be involved in the energy dissipation required for the shocks to exist (Hess et al., 1998; Wilson et al., 2007).

### 2.3.2 Radio bursts

Also related to high solar activity are solar radio bursts. During a radio burst the emission of the solar electromagnetic radiation at radio wavelengths is enhanced. Depending on their signatures, radio burst can be classified into different types. The most relevant in this thesis, are Type II and III radio

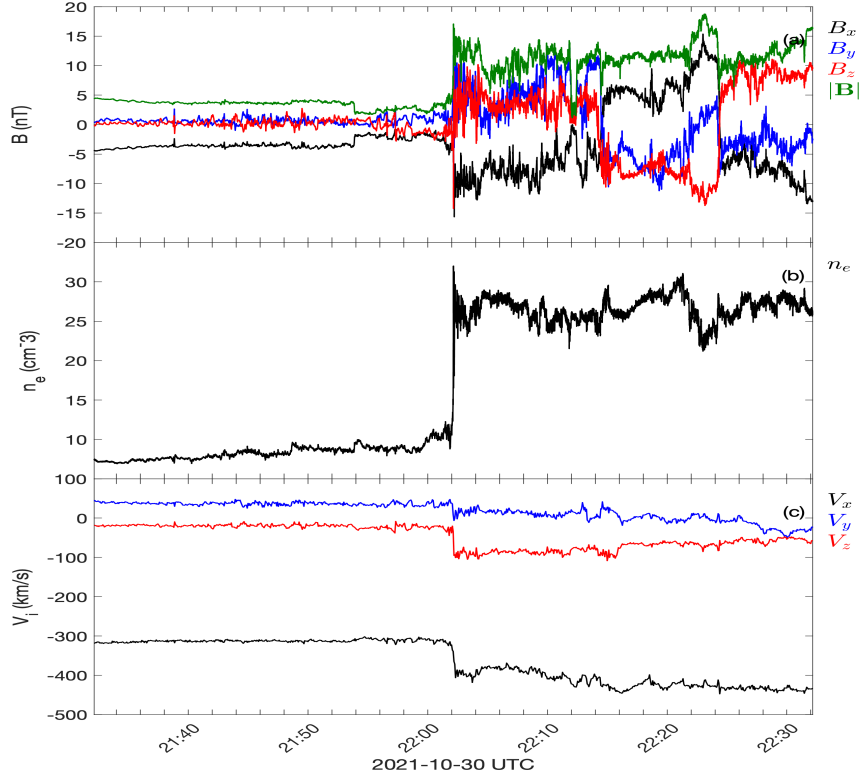


Figure 5: An example of an IP shock as seen by the Solar Orbiter spacecraft, characterized by jumps or discontinuities in density, bulk velocity and magnetic field. The x-axis is toward the Sun, the y-axis points against the spacecraft’s velocity vector and the z-axis is directed normal to the orbital plane of Solar Orbiter. (a) Magnetic field components and magnitude. (b) Density derived from the spacecraft electrostatic potential. (c) Bulk velocity components of the solar wind.

bursts, which are related with CMEs and solar flares, respectively. An example of a Type III radio burst is presented in Fig. 6. They appear as an increase in electromagnetic power density with decreasing frequency.

Solar wind Type II radio bursts are generated when electrons are accelerated upstream of shock waves driven by CMEs, and an electron beam population develops in the distribution function (Ergun et al., 1998). These beams render the distribution unstable, by means of the electron-beam instability described in section 3.3. Subsequently, Langmuir waves are triggered, and through various processes their energy is converted into radio emissions (Gra-



ham & Cairns, 2015). Similarly, Type III radio burst are generated by electrons accelerated by strong convective electric fields near the corona associated with solar flares (Shibata & Magara, 2011). These energetic electrons can escape the corona and excite Langmuir wave emissions in the solar wind. Radio burst have been widely studied due to their relation with Langmuir waves and fast electron beam populations (Lin et al., 1981, 1986; Graham & Cairns, 2015; Mann et al., 2022).

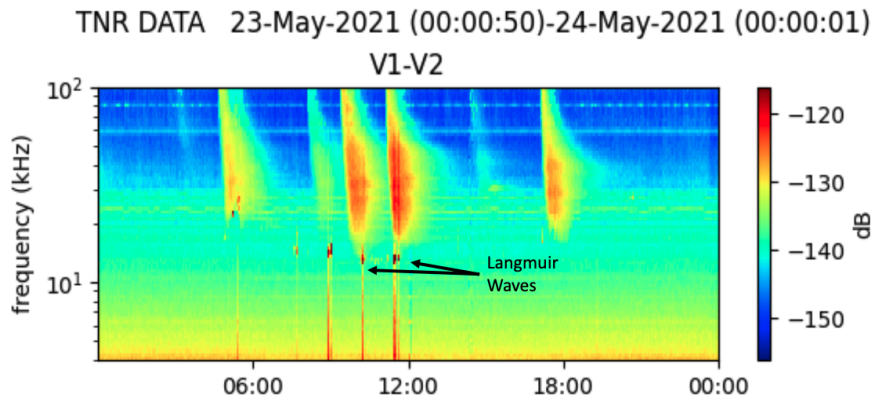


Figure 6: A series of radio bursts captured by Solar Orbiter. The radio burst is recognized by its enhancement in power at radio frequencies. Langmuir waves are observed at the base of the radio burst, close to the electron plasma frequency. Retrieved from: <https://rpw.lesia.obspm.fr/rpw-data/daily-summary-plots/>

### 2.3.3 Magnetic holes

One last solar wind feature relevant for this thesis are magnetic holes. Magnetic holes are defined as localized depressions in the magnetic field magnitude Turner et al. (1977). An example of a solar wind magnetic hole is presented in Fig. 7. The blue crosses indicate the times when Langmuir waves were observed. We note that all of the Langmuir waves in this interval occurred inside the magnetic hole. In section 3.2, we demonstrate that Langmuir occur at frequencies near the electron plasma frequency. Since the electron plasma frequency depends on the density, the electron density can be reliably estimated from the frequency of Langmuir waves. Indeed, we see that the density estimated from Langmuir waves is close to the density obtained from the spacecraft potential shown in red.

Magnetic holes are often in pressure balance with the plasma, and a density enhancement is normally tied to them, as seen in Fig. 7. Their origin is not well understood, but some theories point toward mirror mode storms remnants (Winterhalter et al., 1994). Whatever their origin might be, magnetic holes are frequently found in the solar wind, with sizes around 20 proton gyroradii near Mercury’s orbit (Volwerk et al., 2020). Previous studies suggested that magnetic holes might be source regions of solar wind Langmuir waves (Lin et al., 1995; Briand et al., 2010). Magnetic holes can modify the electron distributions so they can be unstable to Langmuir waves. Langmuir waves might then subsequently affect the electron VDFs.

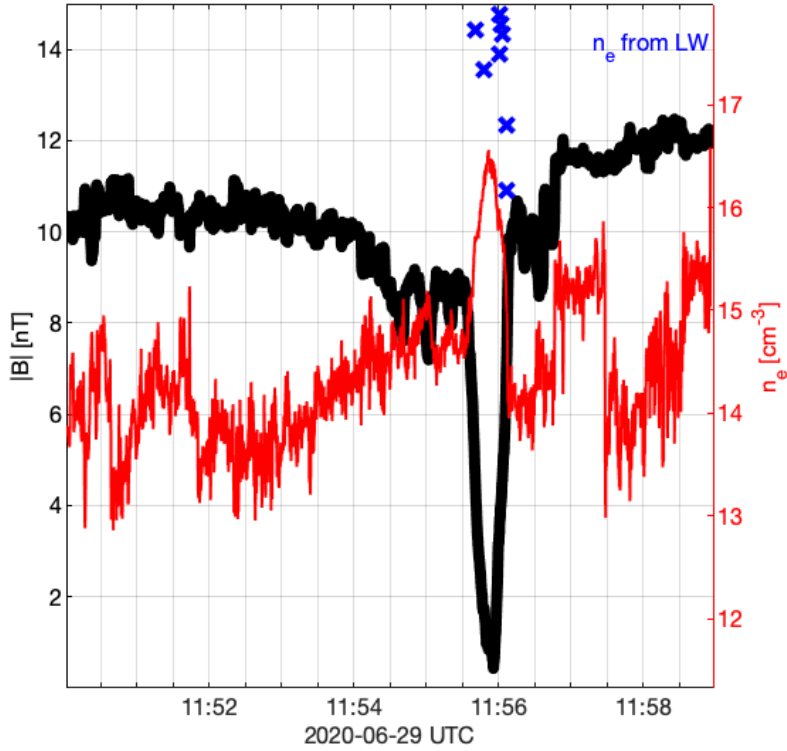


Figure 7: A magnetic hole observed by Solar Orbiter. In the left axis in black, the magnetic hole is characterized by its decrease in magnetic field magnitude. To the right axis in red, the density profile around the magnetic hole. A localized enhancement in density is a common feature of solar wind magnetic holes. The blue crosses indicate the density estimated from Langmuir waves. All of the Langmuir waves observed in this interval occur inside the magnetic hole.



### 3 Plasma Waves

Disturbances from the equilibrium state in an ordinary gas propagate as sound waves, with pressure-gradients acting as the restoring force. As a collection of charged particles, a plasma, reacts to the long-range forces from electric  $\mathbf{E}$  and magnetic fields  $\mathbf{B}$  via the Lorentz force ( $q[\mathbf{E} + \mathbf{v} \times \mathbf{B}]$ ). In addition to pressure gradients, the reaction of plasma particles with electromagnetic fields leads to a variety of new wave modes not present in dielectric media. Since collisions are usually not dominant in the solar wind, processes dictated by interactions between waves and plasma particles might play a primary role in its evolution. In this chapter, we explain the plasma waves that are investigated in this thesis. We start by introducing, in section 3.1, the basic tools required to understand waves in a plasma. In section 3.2, we focus on electrostatic waves, which includes the wave modes investigated in papers I and II. We finish this chapter with section 3.3 explaining possible kinetic instabilities that might give rise to the observed electrostatic waves in the solar wind.

#### 3.1 Basic plasma wave theory

As there are different ways to model a plasma, such as a MHD-fluid, using moment equations or applying kinetic theory, there are various ways to analyze plasma waves. For example, an MHD-fluid approach will only be reliable describing waves at very low frequencies and long length scales. In contrast, kinetic theory can also describe these waves but in far more general and accurate way. The wave modes will also differ if certain assumptions are made. For example, we can consider the plasma as magnetized or unmagnetized; as hot or cold, or with small or large perturbations. Except for the case of large perturbations, wave linear theory can be applied. Nonlinear theory must be applied if the amplitude of the fluctuating quantity is of the same order of magnitude or larger than the background value of that quantity. In this sense, we refer to waves as a small first order propagating fluctuation ( $x_1$ ) of the quantity  $x$  around its equilibrium value ( $x_0$ ). Here,  $x$  represents any dependent variable of the system, for example the magnetic field  $\mathbf{B}$ . In this thesis we focus in hot ( $T \neq 0$ ) kinetic waves with no fluctuating magnetic component ( $\mathbf{B}_1 = 0$ ). Plasma waves with  $\mathbf{B}_1 = 0$  are called electrostatic.

The general approach to deal with linear wave analysis can be summarized in the following steps:

1. **Linearization of the system:** Define the total quantity  $x$  as a zero order background value plus a small amplitude perturbation such that

$$x = x_0 + x_1. \quad (11)$$

The quantity  $x$  may be a part of a coupled system, so disturbances in a quantity will cause changes in all the dependent variables of the system. In the expansion of  $x$ , second order terms and higher are neglected. In MHD we use the fluid equations. Another approach is to linearize the fluid equations from the moments of ions and electrons' VDFs to give a two-fluid description. In kinetic theory the perturbations are applied directly into Vlasov equation (10), such that the VDF consists on a zero-order equilibrium component  $f_{s0}$  and a small-amplitude first-order component  $f_{s1}$  as

$$f_s = f_{s0} + f_{s1}. \quad (12)$$

In all cases, the electromagnetic fields are governed by Maxwell's equations, which are also linearized and need to be self-consistently solved. The linear coupling between the the fields and the response of the plasma can be expressed by Ohm's law:

$$\mathbf{J} = \overleftrightarrow{\sigma} \cdot \mathbf{E}, \quad (13)$$

where  $\mathbf{J}$  is the current density, and  $\overleftrightarrow{\sigma}$  is the conductivity tensor.

2. **Define the form of the disturbance:** Define the disturbance to be a superposition of elementary plane waves  $e^{i(\mathbf{k} \cdot \mathbf{r} - \omega t)}$ . Each component corresponds to a frequency ( $\omega$ ) and a wave propagation vector ( $\mathbf{k}$ ) perpendicular to the planes where the phase is constant. In this way, the planes of constant phase move in the direction of  $\mathbf{k}$  at the phase velocity

$$\mathbf{v}_p = \frac{\omega}{k} \hat{\mathbf{k}} \quad (14)$$

where the magnitude and unit vector of  $\mathbf{k}$  are  $k$  and  $\hat{\mathbf{k}}$ , respectively.

3. **Perform a Fourier transformation:** The system of equations consisting of Maxwell's equation and, either the MHD-fluid equations, the

two-fluid equations, or the Vlasov equation, is a differential equation system with temporal ( $\frac{\partial}{\partial t}$ ) and spatial ( $\nabla$ ) derivative terms. A wave solution  $x_1(\mathbf{r}, t)$  satisfying the linear differential equation

$$D(\nabla, \frac{\partial}{\partial t})x_1 = 0, \quad (15)$$

can be converted into an algebraic equation, by applying a Fourier transform to get

$$D(i\mathbf{k}, -i\omega)\tilde{x}_1 = 0, \quad (16)$$

where  $\tilde{x}_1$  is the Fourier transform of the function  $x_1$ . In this form, it is simpler to determine the valid wave solutions  $x_1$ , than dealing with the derivatives. A non-trivial solution, where a perturbation exist ( $x_1 \neq 0$ ), must satisfy

$$D(i\mathbf{k}, -i\omega) = 0 \quad (17)$$

This condition is called the dispersion relation.

4. **Solve for the roots of  $D(i\mathbf{k}, -i\omega) = 0$ :** From the system of algebraic equations, we obtain the possible solutions of the first order perturbations  $x_1$ , which are found by solving eq. (17). If the system is in matrix form, it is then the determinant of  $\mathbf{D}(i\mathbf{k}, -i\omega)$  that needs to be equal to 0. Solving for the roots of the dispersion relation, will yield a relation between  $\omega$  and  $\mathbf{k}$  providing the wave properties.

In the general case, we look for solutions of waves propagating in a medium with effective dielectric constant  $K$ , which is a tensor  $\overleftrightarrow{\mathbf{K}}$  if the medium is anisotropic. The effective dielectric tensor is related to the conductivity tensor and permittivity of free space in Fourier space as

$$\overleftrightarrow{\mathbf{K}} = [I_{3 \times 3}] - \frac{\overleftrightarrow{\boldsymbol{\sigma}}}{i\omega\epsilon_0}, \quad (18)$$

where the matrix  $I_{3 \times 3}$  is the unit tensor.

In a source-free system, Maxwell's equations can be rearranged in Fourier space to yield the wave homogeneous equation

$$\mathbf{k} \times (\mathbf{k} \times \tilde{\mathbf{E}}_1) + \frac{\omega^2}{c^2} \overleftrightarrow{\mathbf{K}} \cdot \tilde{\mathbf{E}}_1 = 0. \quad (19)$$

The non-trivial roots of the dispersion relation  $D(i\mathbf{k}, -i\omega)\tilde{\mathbf{E}}_1 = 0$  of eq. (19)

provide the possible wave modes that can propagate in the plasma with characteristics given by  $\overleftrightarrow{\mathbf{K}}$ .

### 3.2 Electrostatic waves

We now follow the steps described in the previous section to derive an expression for the dispersion relation of electrostatic kinetic waves. We begin by combining and expanding Vlasov equation (10) of the zeroth and first order quantities, as in eq. (11), and discarding any second order or higher terms. Then, the linearized Vlasov equation is,

$$\frac{\partial f_{s1}}{\partial t} + \mathbf{v} \cdot \nabla f_{s1} + (\mathbf{v} \times \mathbf{B}_0) \cdot \nabla_v f_{s0} + \frac{q_s}{m_s} (\mathbf{v} \times \mathbf{B}_0) \cdot \nabla_v f_{s1} + \frac{q_s}{m_s} [E_1 + \mathbf{v} \times \mathbf{B}_1] \cdot \nabla_v f_{s0} = 0 \quad (20)$$

Where  $E_0 = 0$ , since for the cases we are interested in, it is always possible to transform to a frame where this is true. The velocity  $\mathbf{v}$  is not linearized as it is here an independent variable. Instead of finding the roots of the wave homogeneous equation in eq. (19), several assumptions can be made to simplify the analysis. We can consider pure electrostatic waves, so that there is no fluctuating component of the magnetic field ( $B_1 = 0$ ). Furthermore, we consider a simplified version of the system where  $B_0 = 0$ . Then, the convection term  $\mathbf{v} \times \mathbf{B}_0$  in the Lorentz force vanishes and the electric field can be expressed as  $\mathbf{E} = -\nabla\Phi$ . Where  $\Phi$  is the electrostatic potential and can be calculated using Poisson's equation. This consideration will allow us to describe electrostatic waves in a more instructive way, and with results that can still be applied to the observations.

After these modifications the linearized Vlasov equation (20) is rewritten as

$$\frac{\partial f_{s1}}{\partial t} + \mathbf{v} \cdot \nabla f_{s1} + \frac{q_s}{m_s} \Phi_1 \cdot \nabla_v f_{s0} = 0 \quad (21)$$

and we complete the system by linearizing Poisson's equation

$$\nabla^2 \Phi_1 = -\frac{\rho_{q1}}{\epsilon_0} = -\frac{q_s}{\epsilon_0} \int_{-\infty}^{\infty} f_{s1} d^3v \quad (22)$$

with  $\rho_q$  being the charge density, which is equal to the charge  $q$  multiplied by the zeroth moment of the VDF, i.e. the number density.

The next step is to apply a Fourier transform to the linearized system of eqs. (21) and (22). These equations in Fourier space are respectively

$$-i\omega \tilde{f}_{s1} + ikv_z \tilde{f}_1 + ik \frac{q_s}{m_s} \tilde{\Phi}_1 \frac{\partial f_{s0}}{\partial v_z} = 0 \quad (23)$$

and

$$k^2 \tilde{\Phi}_1 = -\frac{q_s}{\epsilon_0} \int_{-\infty}^{\infty} \tilde{f}_{s1} d^3v \quad (24)$$

We have selected the reference frame so the  $z$ -axis is aligned to the propagation vector. Now, we introduce the reduced VDF  $F_{sz0}$  along this axis. The reduced distribution is normalized by  $n_{s0}$ . Next, we solve for  $\tilde{f}_{s1}$  in eq. (23), substitute it in (24) and combine for a multi-species plasma. After rearranging, the following equation is obtained,

$$D(ik, -i\omega) \tilde{\Phi} = \left[ 1 - \sum_s \frac{\omega_{ps}^2}{k^2} \int_{-\infty}^{\infty} \frac{\partial F_{sz0} / \partial v_z}{v_z - \omega/k} dv_z \right] \tilde{\Phi} = 0. \quad (25)$$

Where  $\omega_{ps}^2 = q_s^2 n_{s0} / \epsilon_0 m_s$  is the species  $s$  plasma frequency. The last step is to find the roots of  $D(ik, -i\omega)$ , however one difficulty arises from it. At phase velocities  $\omega/k = v_z$  the denominator of the integral goes to zero. If there are particles moving at this speed, solutions for  $D(ik, -i\omega)$  cannot be found using Fourier transform alone.

This problem stems from step 2 in our wave analysis. We have implied that a solution of the form  $e^{i(\mathbf{k}\mathbf{r} - \omega t)}$  exists at all times, ignoring any initial transient behavior that may exist. Particles moving at  $\omega/k$  will interact heavily with the wave, regulating its evolution and vice versa. Therefore, the time response of the perturbations needs to be addressed as well. This initial value problem was first resolved by Landau (1946), by taking into account the time evolution of the perturbations using Laplace transformations.

We retake the wave analysis from step 3, but we perform a Fourier transform in space and then a Laplace transform in time to eqs. (21) and (22). Then, eq. (25) is modified and yields an expression of the form

$$D(k, s) \tilde{\Phi}_1 = N(k, s). \quad (26)$$

The complex number  $s = \gamma - i\omega$  is the Laplace space variable. Because now the initial conditions of  $f_{s1}$  are taken into account, a non-zero right-hand side term  $N(k, s)$  appears. Here,  $D(k, s)$  is exactly the same as  $D(ik, -i\omega)$  in (25), but with  $\omega$  replaced by  $is$ .

Solving eq. (26) is an intricate process that involves finding the inverse



Laplace transform of  $\tilde{\Phi}_1$ , which requires the analytical continuation of  $N(k, s)$  and  $D(k, s)$ , because the Laplace transform diverges for values of  $\gamma < 0$ . Making the physically acceptable assumption that  $N(k, s)$  and  $D(k, s)$  are analytical functions, the only poles of  $\tilde{\Phi}_1 = N(k, s)/D(k, s)$ , occur when  $D(k, s) = 0$ . Thus,  $D(k, s)$  plays the same role as the dispersion relation  $D(ik, -i\omega)$  in the Fourier approach. The only difference is that the dispersion relation  $D(k, s)$  is now a function of the complex number  $is$ . The real part ( $\omega = 2\pi/t$ ) corresponds to the actual frequency and the imaginary part ( $i\gamma$ ) to the growth rate. For solutions where  $\gamma < 0$  we have wave damping and for  $\gamma > 0$  we have wave growth.

The dispersion relation  $D(k, s)$  is found after the analytical continuation. Applying the Cauchy residue theorem to find the inverse Laplace transform we obtain

$$D(k, s) = 1 - \sum_s \frac{\omega_{ps}^2}{k^2} \int_C \frac{\partial F_{sz0}/\partial v_z}{v_z - is/k} dv_z, \quad (27)$$

which is similar to eq. (25), but now the integration is over the contour  $C$  enclosing the poles of  $\tilde{\Phi}_1$ . Since  $C$  is closed to infinity in the left hand plane, the poles need to be to the left of the right boundary of the contour in order to be enclosed by it. For poles that lie in the region  $\gamma > 0$  no further action is needed and eq. (27) is valid. If the pole is in the region  $\gamma < 0$ , a distortion of the contour is needed to include the pole that is in the region where the Laplace transform does not exist. The contribution of these poles to eq. (27) is

$$-2\pi i \frac{k}{|k|} \frac{\omega_{ps}^2}{k^2} \frac{\partial F_{sz0}}{\partial v_z} \Big|_{v_z=ip/k}, \quad (28)$$

which is added to  $D(k, s)$ . For the wave onset ( $\gamma = 0$ ) the pole contribution is half of this.

Due to the time response of the perturbations, we now have complex roots of the dispersion relation. This translates to wave modes that are damped or that grow. This collisionless process is called Landau damping (or inverse Landau damping in the latter situation). It is a kinetic process that is not found when working in a fluid framework. It is an important mechanism in which waves can interact with particles moving at the same velocity as the wave in the plasma, i.e  $v_z = \omega/k$ . These particles are said to be resonant with the wave. A simple way to picture this process is to think that at velocities in

the vicinity of  $\mathbf{v}_p$ , slower particles will be accelerated by the wave and the wave will lose momentum, it will be damped. Faster particles will lose momentum and transfer it to the wave, which in turn will grow in amplitude. For a Maxwellian distribution, there are more particles at slower velocities than faster ones near  $\mathbf{v}_p$ . Therefore, waves in a Maxwellian plasma will tend to damp. In weakly collisional plasmas, such as the solar wind, Landau damping may be an important mechanism for transfer of energy between the fields and the particles.

### 3.2.1 Langmuir waves

The last step in our wave analysis is to solve for the roots of  $D(k, s) = 0$  and find the wave modes. When  $\gamma \gg \omega_r$ , the wave amplitude increases in a time shorter than a wave period, the periodic behavior is lost and linear theory is no longer valid. Therefore, the subsequent solutions presented here satisfy the weak growth approximation  $\gamma \ll \omega_r$ .

We begin with Taylor expansion of  $D(k, s)$  around  $s = -i\omega$ . Keeping only first order terms, we get

$$D(k, s) = D_r(k, -i\omega) + iD_i(k, -i\omega) + i\left(\frac{\partial D_r(k, -i\omega)}{\partial \omega}\right)\gamma = 0 \quad (29)$$

Here,  $D_r(k, -i\omega)$  and  $D_i(k, -i\omega)$  indicate the real and imaginary parts of  $D(k, s = -i\omega)$ . Separating the real and imaginary parts we get the following expressions for the dispersion relation and growth rate

$$D_r(k, -i\omega) = 0 \quad (30)$$

$$\gamma = \frac{-D_i(k, -i\omega)}{\partial D_r / \partial \omega} \quad (31)$$

The real part is the usual dispersion relation relating  $\omega$  with  $\mathbf{k}$  and  $\gamma$  is the growth rate predicted by the Landau approach, which is proportional to  $\partial F_{sz0} / \partial v_z$ . Therefore, a positive slope in the reduced distribution will cause growth rate.

Applying this to the dispersion relation in eq. (27), for electrons with Maxwellian distribution, we obtain

$$\omega^2 = \omega_{pe}^2 + 3v_{th,e}^2 k^2 \quad (32)$$

and

$$\gamma = -\sqrt{\frac{\pi}{8}} \frac{\omega_{pe}}{k^3 \lambda_D^3} \exp \left[ -\frac{1}{(2k\lambda_D)^2} - \frac{3}{2} \right]. \quad (33)$$

These equations are the dispersion relation of Langmuir waves. Here, we have considered only electron motion and immobile ions. This means that we are considering perturbations with high frequencies, so the ions cannot respond quickly enough to them, due to their larger mass. This does not mean that the effect of ions is nonexistent, but it is small enough that can be treated as a small correction to the dispersion relation. The dispersion relation of Langmuir waves is plotted in Fig. 8(b). This dispersion relation can be found using different frameworks, such as the moment equations, however they will fail in identifying the damping process that the waves will suffer, as seen from the kinetic approach.

We see from eq. (32), that in the limit of cold electrons ( $v_{th,e} = 0$ ), the frequency is just the electron plasma frequency. This is the frequency at which a plasma will oscillate due to microscopic charge separation. Electric fields generated from these charge separations will act as a restoring force. The effect of electron thermal motion will produce a propagating wave at frequencies close to  $\omega_{pe}$ , these are the Langmuir waves. A spectrogram of electric field waveform snapshots captured by Solar Orbiter is shown in Fig. 8(a). Details of Solar Orbiter's snapshots are given in section 5. The Langmuir waves are identified as emissions close to the electron plasma frequency  $f_{pe}$ . We note that these Langmuir waves are observed in absence of radio bursts signatures. In paper I, we investigate Langmuir waves that are not connected with radio burst source regions, in order to recognize the plasma conditions that make their excitation favorable and understand the role of Langmuir waves in shaping the electron VDFs in the solar wind. An example of a Langmuir waveform is shown in Fig. 8(c). The electric field waveform is closely aligned with the magnetic field, as expected for electrostatic waves. Typical amplitudes for Langmuir waves in the solar wind are  $\sim 1$  mV/m, with some waves, generally the ones associated with radio burst source regions and planetary foreshocks, reaching  $\gtrsim 10$  mV/m (Hess et al., 2011; Briand, 2015).

### 3.2.2 Ion-acoustic waves

For perturbations with frequencies much lower than  $\omega_{pe}$ , the response of ions becomes important. With this in mind we evaluate the electron integral in

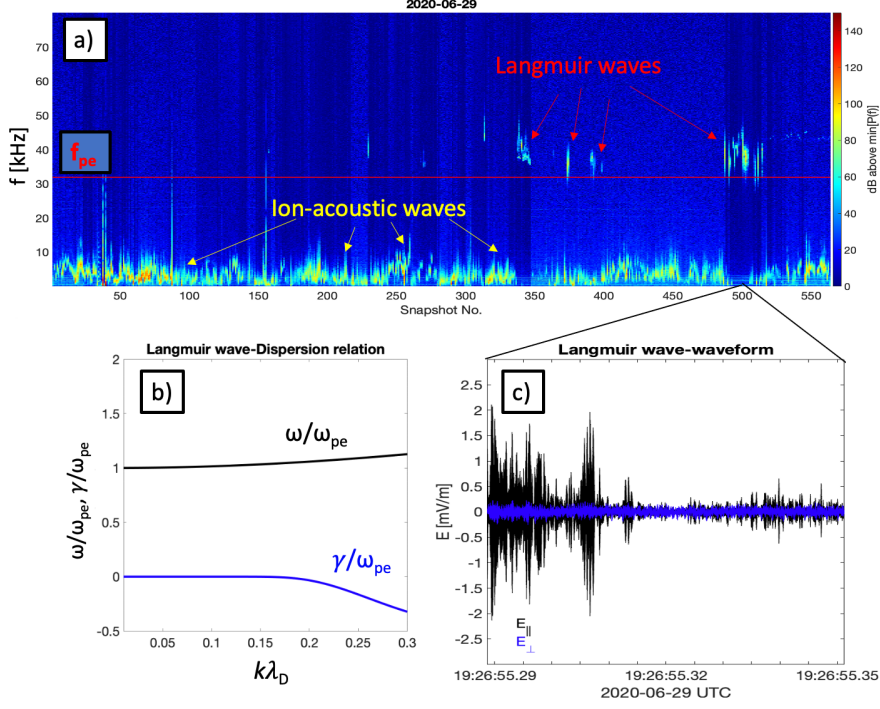


Figure 8: (a) Spectrogram of electric field waveform snapshots captured by Solar Orbiter. Several snapshots are taken every day, the x-axis indicates the snapshot number of the given day. Langmuir waves and ion-acoustic waves are observed on this day. (b) Dispersion relation of Langmuir waves derived from eqs. (32) and (33). At long wavelengths ( $k\lambda_D \ll 1$ ) the frequency of Langmuir waves approaches the electron plasma frequency. (b) Waveform of a Langmuir wave observed by Solar Orbiter. The wave field is mostly along the component parallel to the magnetic field (black). The component perpendicular to the magnetic field (blue) remains near the background level.

the dispersion relation eq. (27) in the limit  $\omega/k \ll v_z$  and the ion integral in the  $\omega/k \gg v_z$  limit.

Next, following the same procedure as done with the Langmuir waves, we solve eqs. (30) and (31). The solutions are

$$\omega^2 = \frac{\omega_{pi}^2}{(1 + 1/k^2\lambda_D^2)} \left[ 1 + \frac{3T_i}{T_e}(1 + k^2\lambda^2) \right] \quad (34)$$

and

$$\gamma = -\sqrt{\frac{\pi}{8}} \frac{\omega}{(1 + k^2\lambda^2)^{3/2}} \left[ \sqrt{\frac{m_e}{m_i}} + \left( \frac{T_e}{T_i} \right)^{3/2} \exp\left(-\frac{T_e}{2T_i(1 + k^2\lambda^2)}\right) \right] \quad (35)$$

This is the dispersion relation for ion-acoustic waves. The plot for the ion-acoustic dispersion relation is shown in Fig. 9(a), for two different values of  $T_e/T_i$ . In this case, the ion term is of a similar form to the electron term in the Langmuir wave dispersion relation. Thus, ions behave somewhat similarly to electrons in the Langmuir mode. However, the resulting wave mode differs significantly from Langmuir waves. The difference comes from the electrons, which react to the low frequency perturbations. At long wavelengths ( $k\lambda_D \ll 1$ ), these waves behave as a sound wave, propagating at the ion sound speed ( $c_{ia} = \sqrt{k_b T_e/m_i}$ ), where the electrons provide the pressure gradient restoring force and the ions the inertia. Hence, the name ion-acoustic.

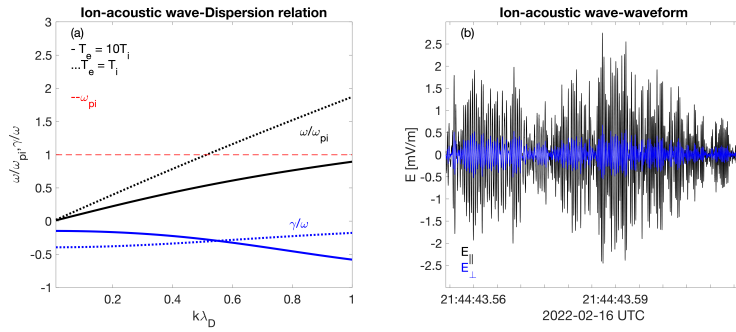


Figure 9: (a) Dispersion relation of ion-acoustic waves derived from eqs. (34) and (35) at two different  $T_e/T_i$  ratios. (b) Waveform of an ion-acoustic wave observed by Solar Orbiter. The wave field is mostly along the component parallel to the magnetic field (black). The component perpendicular to the magnetic field (blue) remains near the background level.

In Fig. 9(b), an example of an ion-acoustic wave is presented. Several ion-acoustic waves are also seen on the spectrogram on Fig. 8(a), with frequencies well below  $f_{pe}$ . The frequency of ion-acoustic waves is near  $\omega_{pi}$ , nevertheless, a spacecraft traveling in the solar wind will observe a shift in frequency. This is because of the convection of the solar wind producing a Doppler shift effect. Solar wind ion-acoustic waves in spacecraft frame vary in frequency from a few hundred Hz up to around 20 kHz at  $\sim 1$  AU (Píša et al., 2021). In contrast, due to their high frequency, the relative Doppler shift felt by Langmuir waves is much less drastic. Ion-acoustic waves are frequently observed in the solar wind (Gurnett & Anderson, 1977; Píša et al., 2021), potentially influencing the various phenomena that occur in the solar wind, such as IP shocks. We study ion-acoustic waves near IP shocks and present our results in paper II. We analyzed the dependence on radial distance of ion-acoustic waves excited in

the upstream and downstream regions of IP shocks. Ion-acoustic waves might be a significant energy dissipation channel for IP shocks and understanding their generation mechanisms and their correlation with shock parameters will provide insight into the physics of IP shocks.

So far, we have assumed that perturbations of certain form exists. However, in order for the perturbation to exist, a source of free energy is necessary. If this is the case an instability can be triggered and wave modes associated to it excited.

### 3.3 Kinetic instabilities

We will now review some instabilities relevant for the excitation of Langmuir and ion-acoustic waves. In the kinetic approach, we look for instabilities related to the VDFs. We mentioned that a particle in resonance with a wave will be accelerated or decelerated, depending if its faster or slower than  $\mathbf{v}_p$ . In thermodynamic equilibrium, there will be more particles moving slower and the net effect is damping. In certain VDF configurations, there may be more particles moving faster than slow ones in the vicinity of  $\mathbf{v}_p$ . In this case, the wave grows in amplitude. A distribution like this will normally have a beam-like population of particles with bulk velocity higher than the core of the distribution. In general, we are looking for distributions with this characteristic, namely with a positive slope ( $\partial F_{sz0}/\partial v_z > 0$ ), as can be seen from eq. (27). We present four examples of instabilities that may explain the observed electrostatic waves in the solar wind.

- **Electron-beam instability:** since ion effects play a minor role in Langmuir wave modes, we typically look for beam-like features in the electron VDF. This instability is called bump-on-tail instability and is one of the strongest candidates for Langmuir wave excitation. This instability depends on the density, temperature and bulk velocity of the beam.
- **Ion-beam instability:** Similarly, for ion-acoustic waves, an ion beam can lead to an instability as well, given that there is a positive slope in the VDF. However, unlike Langmuir waves, the effects of both ions and electrons need to be considered. In particular, electrons can contribute to Landau damping so a positive slope in the ion VDF may not always lead to instability.

- **Current-driven instability:** In the presence of currents due to drifts between ions and electrons, the electron VDF will be shifted with respect to the ion VDF. If the currents are large enough, a positive slope may appear in the equivalent VDF of electrons and ions. The onset of instability will depend on the electron-to-ion temperature ratio  $T_e/T_i$ , the wavelength-to-Debye length ratio  $k\lambda_D$  and the drift-to-ion sound speed ratio  $v_d/c_{ia}$ . This instability will trigger waves of the ion-acoustic type with phase velocities close to  $c_{ia}$ .
- **Heat-flux instability:** Drift velocities can still appear in the absence of net currents. This can be achieved by heat fluxes acting to balance the total current. In the solar wind, heat fluxes are commonly related with non-symmetric features in the distribution function, such as the electron strahl. This velocity drifts will have the same effect as current-induced drifts, generating waves if the equivalent VDF has a positive slope. Since this instability involves a positive slope in the equivalent VDF and non-Maxwellian features, like beams, it is hard to disentangle it from other instabilities in the observations, causing debate regarding their role in the generation of solar wind ion-acoustic waves.

All of the instabilities listed here are associated with a positive slope in the distribution. The first two are related to a bump-on-tail type of distribution, like the example given in Fig. 10(a). The last two, are linked to velocity drifts producing a positive slope in the equivalent distribution of ions and electrons, as shown in Fig. 10(b). Examples of the dispersion relation computed from the distributions on panels (a) and (b) are shown in panels (c) and (d), respectively.

More details regarding these instabilities are presented in papers I and II. We have based our wave analysis on derivations presented in a variety of space plasma physics textbooks, and for a deeper and more rigorous explanation on its derivation, as well a more exhaustive list of wave modes and instabilities, we refer to a few of them, such as (Treumann & Baumjohann, 1997; Gurnett & Bhattacharjee, 2017; Baumjohann & Treumann, 1997; Gary, 1993; Swanson, 1989).

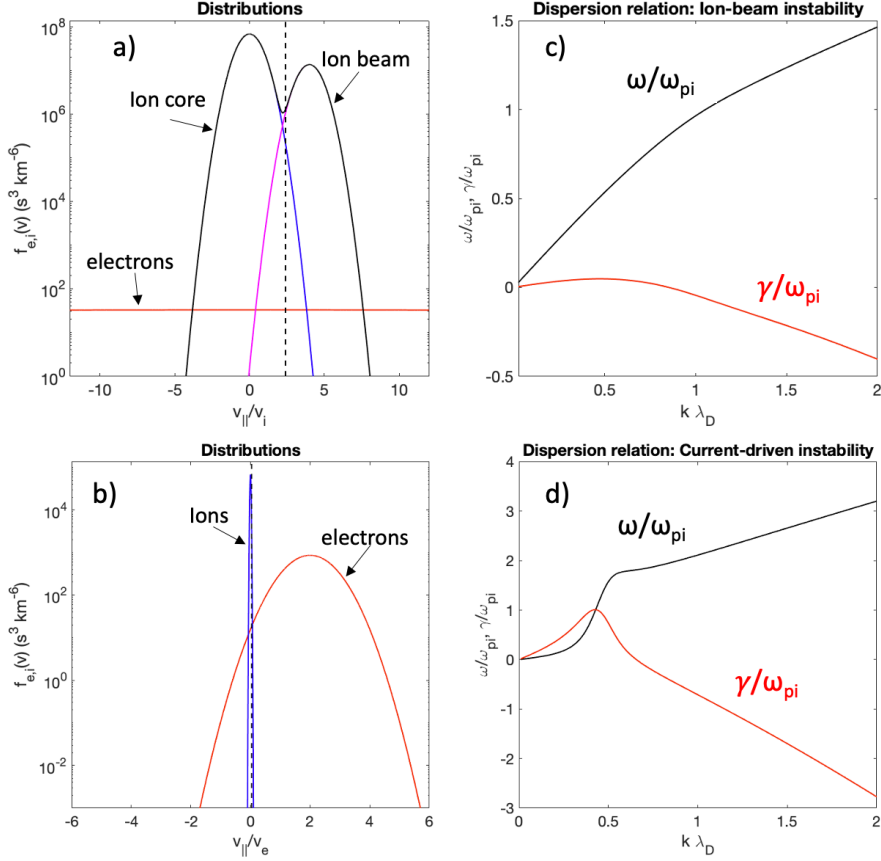


Figure 10: Two examples of distributions subject of different kinetic instabilities. (a) Electron and two ion populations distributions unstable to the ion-beam instability. (b) Ion and drifting electron distributions unstable to the current-driven instability. (c) Dispersion relation calculated from the distribution on panel (a). (d) Dispersion relation calculated from the distribution on panel (b)



## 4 Effect of electrostatic waves on the evolution of the solar wind

The role of kinetic electrostatic waves on the evolution of the solar wind is still debated. In order to provide answers, first we need to know how common electrostatic waves are in the solar wind and how their occurrence varies with distance. Second, it is necessary to know how the waves are triggered and what instabilities and sources of free energy take part in it. In this chapter we briefly discuss some possible effects of Langmuir and ion-acoustic waves on the evolution of the solar wind VDF. We focus in the connection between previous solar wind observations and the results presented in papers I and II.

Solar wind measurements show that the electron VDF changes with helio-centric distance (Maksimovic et al., 2005), as shown in both panels on Fig. 11. In particular, it is theorized that the strahl dissipates into the halo population over distance from the Sun. It is likely that wave-particle interactions are responsible for the observed changes in the solar wind electron VDF. However, which waves are involved remains unresolved. One plausible candidate are Langmuir waves due to their tight relation with electron thermodynamics.

Langmuir waves have been frequently studied in the solar wind in connection with radio bursts (Lin et al., 1981, 1986; Ergun et al., 1998; Graham & Cairns, 2015). However, Langmuir waves, outside of these regions also exist in the solar wind. In paper I, we investigated the occurrence of non-radio burst related Langmuir waves in the solar wind. We analyzed the plasma conditions where these waves were most likely observed and explored possible generation mechanisms. In particular, we found a tight relation with Langmuir waves

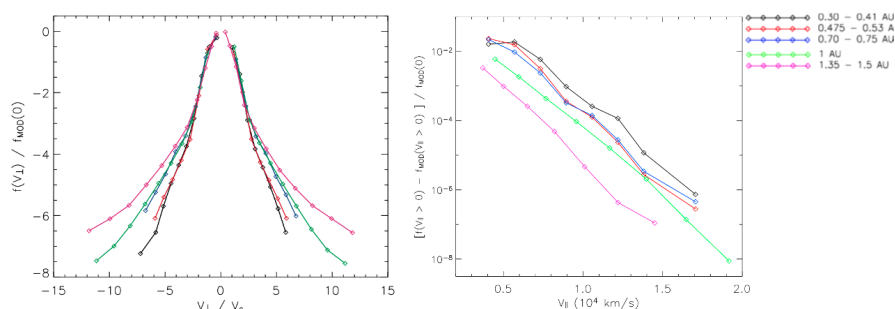


Figure 11: Evolution of the electron distribution function in the inner heliosphere. Left: core and halo components. Right: strahl component. Taken from (Maksimovic et al., 2005)

and magnetic holes, supporting the idea that these magnetic structures are indeed source regions of Langmuir waves in the solar wind.

Besides Langmuir waves, ion-acoustic waves are a common feature of the solar wind in the inner heliosphere. With occurrence rates between 0.1 %- 1 % (Graham et al., 2021; Píša et al., 2021), it is likely that they play some role in shaping the VDFs in the solar wind. Despite being discovered several decades ago (Gurnett & Anderson, 1977), their origin is still disputed. Theories normally revolve around proton beams (Gary, 1978), strong current sheets (Fried & Gould, 1961), electron heat-fluxes (Forslund, 1970) and ion-scale turbulence (Valentini et al., 2011). Understanding the mechanisms that trigger these waves will help us identify what is their effect in the solar wind VDFs.

In paper II, we focus in ion-acoustic waves occurring near IP shocks. Since, shocks require dissipation, in a collisionless environment, the presence of ion-acoustic waves may indicate that an important dissipation mechanism is in place through these waves. Using a list of IP shocks observed by Solar Orbiter at different distances (Dimmock et al., 2023), we found that ion-acoustic activity is enhanced near the ramp of IP shocks, in accordance with previous studies at 1 AU (Hess et al., 1998; Wilson et al., 2007). Furthermore, we observe a slight correlation with ion-acoustic wave occurrence rate near IP shocks and heliocentric distance.

Interplanetary shocks also serve as a laboratory for ion-acoustic wave studies, where the extreme solar wind conditions can highlight the processes involved in the generation mechanisms. In this sense, studying ion-acoustic waves associated with IP shocks may help us understand the role of the waves in the energy dissipation of low-to-moderate  $M$  shocks; as well as identifying sources for solar wind ion-acoustic waves. In particular, we found that estimated currents do not meet the current-driven instability thresholds for wave onset. It is likely that more complex triggering mechanisms may be active, involving a combination of various instabilities and modifying the theoretical thresholds. Knowing which instabilities are important in triggering the electrostatic waves in the solar wind, will reveal what are some of the drivers of the observed evolution of the electron and ion VDFs.

## 5 The Solar Orbiter Mission

Solar Orbiter was launched in February 2020 and since then it has been monitoring the solar wind. It orbits the Sun at distances ranging from 0.28 AU to 1.1 AU. The Solar Orbiter payload consists of six remote-sensing instruments and four in-situ experiments (Müller et al., 2020). The allocation of the instruments onboard Solar Orbiter is shown in Fig. 12. To investigate the electrostatic waves in the solar wind we utilized the Radio and Plasma Waves instrument (RPW). For the particle measurements the Solar Wind Analyzer (SWA) instrument was mainly used and the Energetic Particle Detector (EPD) to a lesser extent. Magnetic field data was retrieved from the Magnetometer (MAG) instrument.

Solar Orbiter is a three-axis stabilized spacecraft, with its x-axis always oriented toward the Sun. Its y-axis is anti-parallel to the velocity vector and its z-axis is normal to the orbit plane, completing the spacecraft reference frame (SRF) as depicted in Fig. 12. In this chapter, we will briefly describe the instruments used and how the data is handled.

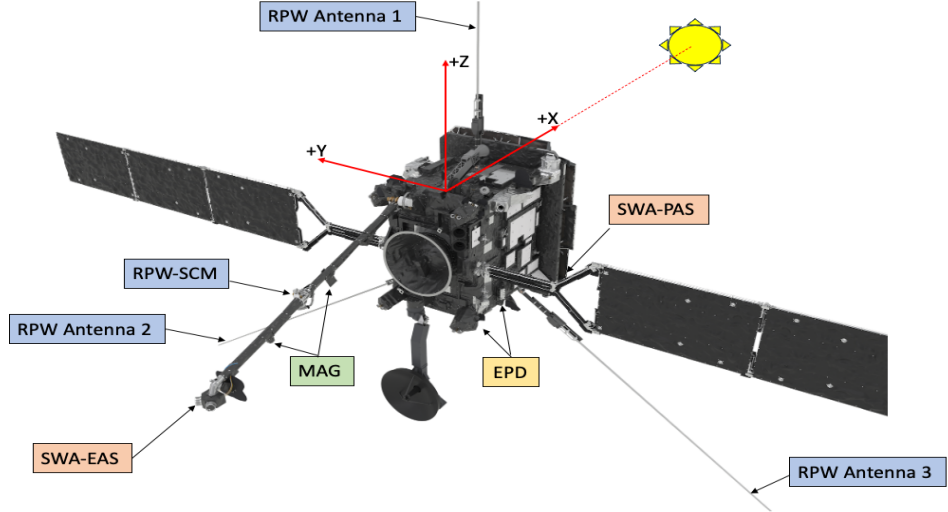


Figure 12: Solar Orbiter spacecraft in-situ experiments and spacecraft reference frame configuration. The x-axis points toward Sun, y-axis points opposite to the velocity vector and the z-axis perpendicular to the orbital plane, completing the right-hand triad. Adapted from <https://www.esa.int/ScienceExploration/SpaceScience/SolarOrbiter>

## 5.1 The Radio and Plasma Waves Instrument

The main source of observations analyzed in this thesis is the RPW instrument suite (Maksimovic et al., 2020). Capable of detecting electric fields from  $\sim$ DC values up to tens of MHz, RPW is well suited to detect electrostatic waves in the solar wind. Besides electric field, RPW also provides electron density derived from spacecraft potential measurements. This instrument consists of a set of three antennae of 6.5 m each, located in the spacecraft's yz-plane and a search coil magnetometer (SCM).

The electric field measurements are processed by four different units, covering different frequency ranges. The Low Frequency Receiver (LFR) handles signals from near DC to approximately 10 kHz. The Thermal Noise Receiver (TNR) and High Frequency Receiver (HFR), focused mainly in observations of radio waves, cover frequencies ranging from 4 kHz to 16 MHz. In the middle frequencies, between 200 Hz and 200 kHz, the Time Domain Sampler (TDS) provides electric field signals in the form of high-resolution snapshots.

With solar wind Langmuir waves ranging around 20 kHz to 60 kHz (Hess et al., 2011; Briand, 2015) and Doppler shifted ion-acoustic waves from few hundred Hz to  $\sim$ 20 kHz (Píša et al., 2021), TDS temporal resolution is sufficient to capture them. The waveform snapshots produced by TDS are typically sampled at 262.1 kHz and with a duration of  $\sim$ 60 ms. The Langmuir and ion-acoustic wave snapshots shown in Figs. 8(a) and 9(b), respectively, were captured by TDS. Snapshots are regularly taken by TDS every minute, but only the ones with highest quality flag are downlinked to the ground station.

Since the telemetry bandwidth does not allow for transmission of all snapshot waveforms, a different data product containing statistical averages is generated onboard. This statistical data (STAT) product, provides median frequency, maximum amplitude, RMS amplitude, among other quantities of snapshots containing waves in a 16 s interval. Since one snapshot is processed every minute, the maximum number of waves a STAT packet can have is 16. A snapshot is classified as containing a wave if it meets the onboard wave algorithm criteria. In this way, continuous data of waves is available, making the STAT product useful for statistical studies. For more details on the onboard wave detection algorithm see Soucek et al. (2021).

## 5.2 Other in-situ experiments

Magnetic field data is available through MAG. This instrument consist of a three-axis fluxgate magnetometer mounted on the same boom as the EAS sensor heads (Horbury et al., 2020). In normal operation mode MAG delivers 8 vectors per second, and 64 vectors per second in burst mode. It has a dynamic range of  $\pm 128$  nT and nominal resolution of 4 pT. With the magnetic field measurements we can probe the solar wind conditions around regions with high wave activity. For example, we can investigate if the electrostatic waves are correlated to magnetic structures such as magnetic holes. We can also represent the VDF by its component parallel and perpendicular to the magnetic field, revealing important features linked to kinetic instabilities. Furthermore, with magnetic field measurements it is possible to perform polarization analysis of the waves, which can provide insight into the waves' nature.

Since we are interested in kinetic waves, information on the particle VDFs is of high interest. Solar Orbiter's SWA can produce VDFs and calculate moments of ions and electrons (Owen et al., 2020). The Proton-Alpha Sensor (PAS), part of the SWA instrument suite, is an electrostatic analyzer that measures 3D ion distributions from 200 eV to 20 keV. Generally, PAS measures a 3D distribution every 4 s, over nine elevation angles, eleven azimuthal angles and 96 energy channels. The instrument does not have a full sky field of view, but its detector opening is directed toward the Sun. This enables the solar wind ion VDF accurately to be resolved, as ions in the solar wind tend to have much larger bulk velocity than thermal velocity.

The electron VDFs are provided by the Electron Analyzer System (EAS), also part of the SWA consortium. Electrons in the solar wind, generally, have larger thermal velocity than bulk velocity, therefore a full sky field of view is required. To address this, EAS counts with two electrostatic analyzer sensor heads mounted on a boom in the shadow of the spacecraft. The cadence of EAS is, nominally, 4 s and it is designed to measure electrons with energies from a few eV to  $\sim 5$  keV. The two sensor heads measurements are combined to generate 3D distributions. Then, these measurements can be used to calculate distributions of particles according to the angle that their velocity vector makes with the magnetic field. This angle is the pitch angle, and the distribution of particles according to their pitch angle is the pitch angle distribution (PAD). These type of distributions are useful for inspection of non-Maxwellian features in the VDF, for example the electron strahl, which can be responsible of

instabilities in the solar wind.

When particles with higher energy than the resolved by SWA are of interest, we make use of EPD. This instrument is capable of detecting energetic particle fluxes with energies around a few keV up to several MeV (Rodríguez-Pacheco et al., 2020). With EPD data we can analyze energetic populations that may influence the instability thresholds. For example, it can be used to find signatures of reflected ions at IP shocks. This backstreaming population of ions can potentially generate ion-acoustic waves, through the ion beam instability (Goodrich et al., 2019).

## 6 Outlook

We have quantified the presence of Langmuir waves in the solar wind and identified possible source regions. Although, generation mechanisms have not been explicitly found, it is likely that the bump-on-tail instability plays a primary role. As described in paper I, Langmuir waves in the solar wind are more common in regions with localized density enhancements with respect to the steady background value. Consequently, instabilities associated with density fluctuations can also be involved. Future developments should focus on case studies of solar wind Langmuir waves not connected to radio bursts in order to confirm the mechanisms behind their excitation.

With the results of paper I, we aim to characterize the Langmuir waves in the solar wind and estimate the overall effect that they might have in the solar wind VDF evolution. Through wave-particle interactions, such as Landau resonance, Langmuir waves may be responsible of a fraction of the observed strahl dissipation into the halo and electron temperature regulation.

Similar analysis should be performed in regard of ion-acoustic waves. In particular, their originating mechanisms must be decoded. Especially, the possible connection of non-Maxwellian VDFs, currents and heat fluxes in the generation of ion-acoustic waves near IP shocks, as suggested in paper II. If such connection exists, it would be possible to test if it holds for regions devoid of IP shocks.

Concerning IP shocks, the energy dissipation provided by ion-acoustic waves must also be assessed. The identification of ion-acoustic wave generation mechanisms near IP shocks, will facilitate distinguishing between the waves related to the shock and the ones related to marginally stable solar wind conditions or other external factors. As a consequence, we may be able to quantify the effects of ion-acoustic waves on energy dissipation at IP shocks.

Furthermore, other possible generation mechanisms of ion-acoustic waves in the upstream and downstream regions of IP shocks must be explored. For instance, recent studies have reported the presence of a backstreaming ion population in the upstream region of an IP shock event (Dimmock et al., 2023). The role that reflected ion beams can play in upstream ion-acoustic wave generation must be investigated. In this manner, it should be possible to link reflected ion beams with observed changes in the upstream VDFs, by means of the beam susceptibility to generate ion-acoustic waves. Impulsively reflected

ions have been proposed as a source of ion-acoustic waves upstream the Earth's bow shock (Goodrich et al., 2019). Its applicability to IP shocks still needs to be addressed. Regarding the downstream region, it still remains unresolved if the ion-acoustic waves observed are generated locally or convected from the ramp. As part of the ongoing study presented in paper II, we will investigate the decay time of the observed ion-acoustic waves and analyze if these waves are indeed convected waves originated at the ramp.

Besides ion-acoustic and Langmuir waves, other kinetic waves, such as, whistlers, ion-cyclotron and electromagnetic ion-cyclotron (EMIC) waves might contribute to the solar wind evolution. Investigation of these waves is also necessary to characterize the different effects of wave-particle interactions in the solar wind VDFs.

Finally, any solar wind model should be able to explain the preferential heating of ions in directions perpendicular to the magnetic field ( $T_{\perp} > T_{\parallel}$ ) in the inner heliosphere. If ion-acoustic waves take part in such process, investigation of the effects of the waves on the ion VDFs may reveal it.



## 7 Acknowledgements

I want to thank Daniel for his support and patience. I also thank Mats, Yuri and Michiko for their feedback and valuable time invested in my learning. I also thank Konstantin, Ida, Josh, Louis, Ahmad who have been always willing to help me when needed. I also thank Myriam, Göran, Linnea, Coco, Jaume, Macarena, Jorge, Monika, Montse, Caro, Camino, Feri, Jose Luis, Ceci, Norma, Andres, Daniel, Ivan, Manolo, Konrad, Katerina, Andersson, Rafa, Andrew, Fredrik, Luca, Andres L, Sebas, Juan Pa, Osiris, Paco, Yayos etc. and of course God.

## References

- Alterman, B. L., Kasper, J. C., Stevens, M. L., & Koval, A. 2018, *The Astrophysical Journal*, 864, 112
- Babcock, H. W. 1961, , 133, 572
- Baker, D. & Kanekal, S. 2008, *Journal of Atmospheric and Solar-Terrestrial Physics*, 70, 195
- Bame, S. J., Asbridge, J. R., Feldman, W. C., Montgomery, M. D., & Kearney, P. D. 1975, *Solar Physics*, 43, 463
- Baumjohann, W. & Treumann. 1997, *Basic Space Plasma Physics*, 1st edn. (Imperial College Press)
- Briand, C. 2015, *Journal of Plasma Physics*, 81, 325810204
- Briand, C., Soucek, J., Henri, P., & Mangeney, A. 2010, *Journal of Geophysical Research: Space Physics*, 115
- Chamberlain, J. 1961, *Astrophysical Journal*, 133, 675
- Chapman S., Z. H. 1957, *Smithsonian Contributions to Astrophysics*, 2
- Council, N. R. et al. 2004, *Plasma physics of the local cosmos*
- Cranmer, S. 2012, *Space Science Reviews*, 172, 145
- Cranmer, S. R., Matthaeus, W. H., Breech, B. A., & Kasper, J. C. 2009, *The Astrophysical Journal*, 702, 1604
- Dikpati, M., Suresh, A., & Burkepile, J. 2016, *Solar Physics*, 291, 339
- Dimmock, A. P., Gedalin, M., Lalti, A., et al. 2023, *Astronomy Astrophysics*
- Eddington, A. S. 1910, *Monthly Notices of the Royal Astronomical Society*, 70, 442
- Ergun, R. E., Larson, D., Lin, R. P., et al. 1998, *The Astrophysical Journal*, 503, 435
- Feldman, W. C., Asbridge, J. R., Bame, S. J., & Montgomery, M. D. 1974, *Reviews of Geophysics*, 12, 715
- Fitzenreiter, R. J. 2003, *Journal of Geophysical Research*, 108, 1415
- Forslund, D. W. 1970, *Journal of Geophysical Research*, 75, 17
- Fried, B. D. & Gould, R. W. 1961, *The Physics of Fluids*, 4, 139
- Gary, S. P. 1978, *Journal of Geophysical Research: Space Physics*, 83, 2504
- Gary, S. P. 1993, *Theory of space plasma microinstabilities*, 1st edn. (Cambridge University Press)
- Goodrich, K. A., Ergun, R., Schwartz, S. J., et al. 2019, *Journal of Geophysical Research: Space Physics*, 124, 1855

- Gosling, J. T., Borrini, G., Asbridge, J. R., et al. 1981, *Journal of Geophysical Research: Space Physics*, 86, 5438
- Graham, D. B. & Cairns, I. H. 2015, *Journal of Geophysical Research: Space Physics*, 120, 4126
- Graham, D. B., Khotyaintsev, Y. V., Vaivads, A., et al. 2021
- Gringauz, KI., B. V. O. V. R. R. 1960, *Sov Phys Dokl*, 5
- Gurnett, D. A. & Anderson, R. R. 1977, *Journal of Geophysical Research*, 82, 632
- Gurnett, D. A. & Bhattacharjee, A. 2017, *Introduction to Plasma Physics: With Space, Laboratory and Astrophysical Applications*, second edition edn. (Cambridge University Press)
- Hansteen, V.H., V. M. 2012, *Space Sci Rev*, 172, 89–121
- Hazra, S. & Nandy, D. 2016, *The Astrophysical Journal*, 832, 9
- Hess, R. A., MacDowall, R. J., Goldstein, B., Neugebauer, M., & Forsyth, R. J. 1998, *Journal of Geophysical Research: Space Physics*, 103, 6531
- Hess, S. L. G., Malaspina, D. M., & Ergun, R. E. 2011, *Journal of Geophysical Research: Space Physics*, 116, n/a
- Horbury, T. S., O'Brien, H., Blazquez, I. C., et al. 2020, *Astronomy Astrophysics*, 642, A9
- Hundhausen, A. J. 1972, *Coronal Expansion and Solar Wind*, Vol. 5 (Springer), 94–121
- Jockers, K. 1970, *Astronomy and Astrophysics*, 6, 219
- Kilpua, E. K. J., Lumme, E., Andreeva, K., Isavnin, A., & Koskinen, H. E. J. 2015, *Journal of Geophysical Research: Space Physics*, 120, 4112
- Landau, L. 1946, *Zhurnal eksperimentalnoi i teoreticheskoi fiziki*, 16, 574
- Leer, E., H. T. E. F. T. 1982, *Space Sci Rev*, 33, 161
- Lemaire, J., S. M. 1971, *Journal of Geophysical Research*, 76, 7479
- Lin, N., Kellogg, P. J., MacDowall, R. J., et al. 1995, *Geophysical Research Letters*, 22, 3417
- Lin, R. P., Levedahl, W. K., Lotko, W., Gurnett, D. A., & Scarf, F. L. 1986, , 308, 954
- Lin, R. P., Potter, D. W., Gurnett, D. A., & Scarf, F. L. 1981, , 251, 364
- Low, B. C. 1996, *Solar Physics*, 167, 217
- Lyons, L. 2003, *Space Plasma Physics* (Elsevier), 577–591
- Maksimovic, M., Bale, S. D., Chust, T., et al. 2020, *The Solar Orbiter Radio and Plasma Waves (RPW) instrument*

- Maksimovic, M., Pierrard, V., & Riley, P. 1997, *Geophysical Research Letters*, 24, 1151
- Maksimovic, M., Zouganelis, I., Chaufray, J., et al. 2005, *Journal of Geophysical Research: Space Physics*, 110
- Mann, G., Vocks, C., & Warmuth, A. 2022, *Astronomy & Astrophysics*, 660, A91
- Marsch, E. 2006, *Living Reviews in Solar Physics*, 3
- Marsch, E. 2018, *Annales Geophysicae*, 36, 1607
- Matteini, L., Landi, S., Hellinger, P., et al. 2007, *Geophysical Research Letters*, 34, L20105
- McComas, D. J., Bame, S. J., Barraclough, B. L., et al. 1998, *Geophysical Research Letters*, 25, 1
- McComas, D. J. ; Velli, M. . L. W. S. . A. L. W. . B.-P. M. . B. V. . D. R. B. . F. W. C. . G. G. . H. S. R. s. b. o. . H. D. M. . M. I. . M. W. H. . M. R. L. . M. R. A. . M. N. . O. L. . S. E. C. . S. C. W. . Z. T. H. 2007, *Reviews of Geophysics*, 45
- Müller, D., Cyr, O. C. S., Zouganelis, I., et al. 2020, *Astronomy & Astrophysics*, 642, A1
- Neugebauer, M. & Snyder, C. W. 1962, *Science*, 138, 1095
- Newbury, J. A., Russell, C. T., Phillips, J. L., & Gary, S. P. 1998, *Journal of Geophysical Research: Space Physics*, 103, 9553
- Ogilvie, K. W. 1975, *Journal of Geophysical Research*, 80, 1335
- Owen, C. J., Bruno, R., Livi, S., et al. 2020, *Astronomy & Astrophysics*, 642, A16
- Parker, E. N. 1958, *Astrophysical Journal*, 128, 664
- Píša, D., Souček, J., Santolík, O., et al. 2021
- Richardson, I. G. 2018, *Living Reviews in Solar Physics*, 15, 1
- Rodríguez-Pacheco, J., Wimmer-Schweingruber, R. F., Mason, G. M., et al. 2020, *Astronomy & Astrophysics*, 642, A7
- Rosenbauer, H., Schwenn, R., Marsch, E., et al. 1977, *Journal of Geophysics Zeitschrift Geophysik*, 42, 561
- Russell, C. T. 2013, *Solar Wind and Interplanetary Magnetic Field: A Tutorial*, 73–89
- Shibata, K. & Magara, T. 2011, *Living Reviews in Solar Physics*, 8
- Soucek, J., Píša, D., Kolmasova, I., et al. 2021, *Astronomy and Astrophysics*, 656

- Swanson, D. G. 1989, *Plasma Waves*, 1st edn. (Academic Press)
- Sweet, P. A. 1969, *Annual Review of Astronomy and Astrophysics*, 7, 149
- Treumann, R. A. & Baumjohann, W. 1997, *Advanced Space Plasma Physics*, first edition edn. (Imperial College Press)
- Turner, J. M., Burlaga, L. F., Ness, N. F., & Lemaire, J. F. 1977, *Journal of Geophysical Research*, 82, 1921
- Valentini, F., Perrone, D., & Veltri, P. 2011, *Astrophysical Journal*, 739
- Velli, M. 1994, *Astrophysical Journal Letters*, 432, L55
- Verscharen, D., Klein, K. G., & Maruca, B. A. 2019, The multi-scale nature of the solar wind
- Volwerk, M., Goetz, C., Plaschke, F., et al. 2020, *Annales Geophysicae*, 38, 51
- Weber, E. J. & Davis, Leverett, J. 1967, , 148, 217
- Wilson, L. B., Cattell, C., Kellogg, P. J., et al. 2007, *Physical Review Letters*, 99
- Winterhalter, D., Neugebauer, M., Goldstein, B. E., et al. 1994, *Journal of Geophysical Research: Space Physics*, 99, 23371
- Zhao, X. & Hundhausen, A. J. 1981, *Journal of Geophysical Research: Space Physics*, 86, 5423
- Štěpán Štverák, Maksimovic, M., Trávníček, P. M., et al. 2009, *Journal of Geophysical Research: Space Physics*, 114